

Effects of Vegetation Clumping on Two-Source Model Estimates of Surface Energy Fluxes from an Agricultural Landscape during SMACEX

MARTHA C. ANDERSON AND J. M. NORMAN

Department of Soil Science, University of Wisconsin—Madison, Madison, Wisconsin

WILLIAM P. KUSTAS AND FUQIN LI

Hydrology and Remote Sensing Laboratory, ARS, USDA, Beltsville, Maryland

JOHN H. PRUEGER

National Soil Tilth Laboratory, Ames, Iowa

JOHN R. MECIKALSKI

National Space Science and Technology Center, University of Alabama at Huntsville, Huntsville, Alabama

(Manuscript received 20 July 2004, in final form 5 April 2005)

ABSTRACT

The effects of nonrandom leaf area distributions on surface flux predictions from a two-source thermal remote sensing model are investigated. The modeling framework is applied at local and regional scales over the Soil Moisture–Atmosphere Coupling Experiment (SMACEX) study area in central Iowa, an agricultural landscape that exhibits foliage organization at a variety of levels. Row-scale clumping in area corn- and soybean fields is quantified as a function of view zenith and azimuth angles using ground-based measurements of canopy architecture. The derived clumping indices are used to represent subpixel clumping in Landsat cover estimates at 30-m resolution, which are then aggregated to the 5-km scale of the regional model, reflecting field-to-field variations in vegetation amount. Consideration of vegetation clumping within the thermal model, which affects the relationship between surface temperature and leaf area inputs, significantly improves model estimates of sensible heating at both local and watershed scales in comparison with eddy covariance data collected by aircraft and with a ground-based tower network. These results suggest that this economical approach to representing subpixel leaf area heterogeneity at multiple scales within the two-source modeling framework works well over the agricultural landscape studied here.

1. Introduction

Leaf area index (LAI) is a key input to remote sensing models of land surface energy balance and carbon exchange because vegetation plays an important role in modulating these fluxes. It has become evident that the way in which leaf area is distributed over a model grid cell, whether homogeneously or clumped, can also be important to some model evaluations. Productivity estimates, for example, may be affected by clumping because of a reduction in the canopy light-capturing ca-

capacity in comparison with that of homogeneous canopies (Nouvellon et al. 2000; Chen et al. 2003). Subpixel heterogeneity in leaf area distribution can also influence model partitioning of available energy because of nonlinearities inherent in land–atmosphere interactions, advection effects, and mismatch with other remote sensing inputs (e.g., Bonan et al. 1993; Blyth 1995; Giorgio and Avissar 1997; Koster and Suarez 1992a; Kustas and Norman 2000a).

Several approaches to accommodating subpixel heterogeneity (here, focusing on LAI) in land surface models have been explored in the literature. One is the “patch” or “mosaic” approach, where a grid cell is segregated into patches of effectively uniform conditions, fluxes are computed independently for each patch, and

Corresponding author address: M. C. Anderson, 1525 Observatory Dr., University of Wisconsin—Madison, Madison, WI 53706.
E-mail: mcanders@facstaff.wisc.edu

the patch fluxes are then aggregated over the cell (e.g., Avissar and Pielke 1989; Koster and Suarez 1992b; Blyth 1995). Another uses a probability density function describing the expected variability in a given land surface parameter over the grid cell (Avissar 1991, 1992). A third approach to treating heterogeneity in LAI is to incorporate a “clumping index” into equations governing surface temperature partitioning, radiative transport through the canopy, and canopy wind penetration (Kustas and Norman 1999a,b). The latter has the advantage of being relatively simple and generic, applying the same equation set for both clumped and homogeneous canopies without significant demand for detailed subpixel information (other than a bulk assessment of clumping). However, while the clumping index approach has been successfully applied to relatively small-scale patchiness (e.g., row crops or forest canopies at the 10^0 – 10^2 m scale), it is not clear whether it can be successfully extended to larger-scale heterogeneity (e.g., field-scale patchiness over 10^3 m scales).

Thermal remote sensing models can be particularly sensitive to inhomogeneous distributions of vegetation because clumping affects the relationship between temperature and cover information and the overall energy balance. In general, vegetation (relatively cool) is better coupled with the atmosphere than is the underlying soil substrate (generally hotter), and, therefore, the contribution of a scene component to the system’s sensible heat flux is not necessarily in proportion to its contribution to the composite surface temperature. In cells with significant clumping, more soil is visible to the thermal sensor than the scene-averaged LAI would suggest, and sensible heating may be overestimated. Vegetation clumping will also modify the functional dependence of apparent surface temperature on view angle, which is caused by the variable obscuration of the underlying bare soil when a canopy is viewed off nadir (Vining and Blad 1992). The strength of this angular dependence will depend on the spatial scale of clumping, whether the bare patches are larger or smaller than the typical canopy height (e.g., Blyth 1995).

In this paper, we study the effects of vegetation clumping in an agricultural landscape on energy partitioning in a thermal-based flux model, and explore the efficacy of the clumping index approach at resolutions of 30 m–5 km. The two-source model (TSM) of Norman et al. (1995) has been successfully implemented over a range of spatial scales—at local scales, using in situ measurements of model boundary conditions (Norman et al. 1995; Kustas and Norman 1997, 1999a,b, 2000b; Li et al. 2005); at regional scales, using an atmospheric boundary layer (ABL) model for energy closure

(Anderson et al. 1997; Mecikalski et al. 1999); and at intermediate scales, using boundary conditions provided by the regional model (Norman et al. 2003; Anderson et al. 2004b). The core two-source (soil + vegetation) representation gives these models flexibility to simulate a much wider range in vegetation cover fraction and thermal sensor view angle than can be accommodated by comparable one-source models (see discussion in Norman et al. 1995; Zhan et al. 1996; Anderson et al. 1997).

This study uses ground-, aircraft-, and satellite-based data collected during the Soil Moisture Experiment 2002 (SMEX02) and the related Soil Moisture–Atmosphere Coupling Experiment (SMACEX; Kustas et al. 2005), which ran concurrently within the Walnut Creek (WC) watershed just south of Ames, Iowa (Fig. 1). As part of SMACEX, surface energy fluxes were measured continuously at eddy covariance (EC) towers that were distributed across the study area, and periodically along tracks flown by research aircraft. Intensive measurements of vegetation cover, height, and LAI were acquired at 31 sampling sites across the watershed. In addition, thermal-infrared (TIR) and visible (VIS)/near-infrared (NIR) imagery from the Geostationary Operational Environmental Satellite (GOES) and Landsat were archived throughout the experiment.

The rapidly evolving mosaic of corn- and soybean fields covering the WC study area provides a good test bed for examining effects of subpixel clumping at several levels of organization. On the Landsat thermal pixel scale (60–120 m), subpixel clumping occurs on the scale of crop rows prior to canopy closure. On the GOES pixel scale (5–10 km), vegetation clumping is manifested at the field scale because of differences in crop type and planting date, particularly in the early phases of crop development before full cover is attained uniformly across the watershed (Fig. 1). With the SMEX02/SMACEX datasets, we explore whether accounting for clumping is necessary within the multiscale TSM modeling suite. Techniques for characterizing vegetation clumping in routine, regional-scale applications are discussed, including using multiangle satellite measurements relating to canopy structure. The operational efficacy of these techniques will be explored in future papers.

2. Model description

a. The two-source model (homogeneous canopy)

With the two-source approximation, the composite directional radiometric temperature [$T_{\text{RAD}}(\theta)$] of a heterogeneous scene is partitioned into soil and canopy contributions (T_s and T_c) in proportion to the fractional

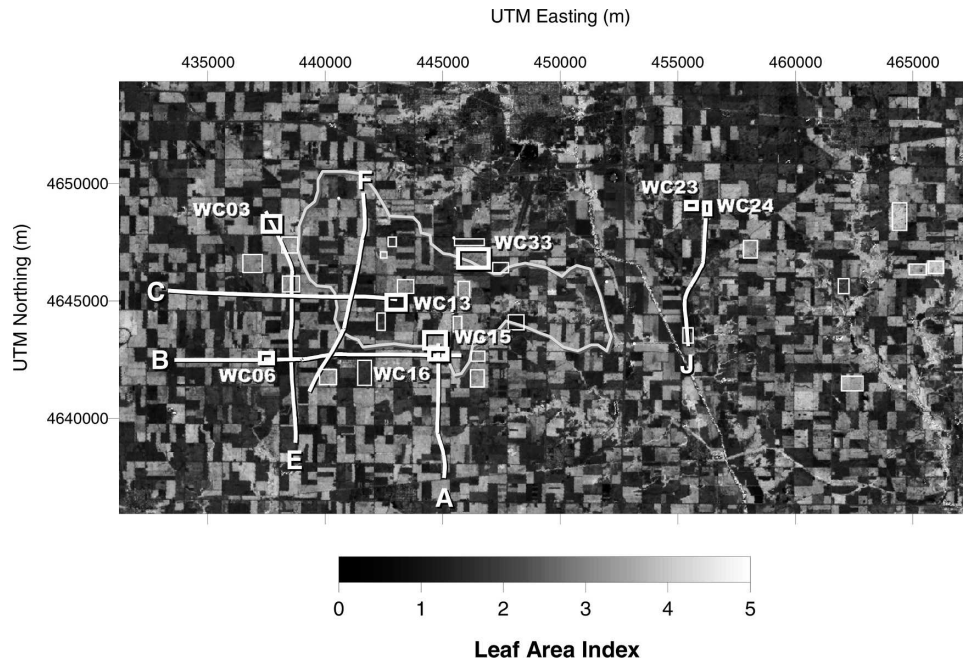


FIG. 1. Map of leaf area index over the Walnut Creek watershed (demarcated in gray), retrieved from multispectral Landsat imagery from 1 Jul 2002. In general, the lower LAI fields on this date are soybean, while higher LAI fields are corn. Rectangles locate fields where intensive vegetation data were collected. EC data used in this study were from towers sited in eight of these fields (denoted with thicker rectangles; sites WC15 and WC16 had two towers each). Lines designate tracks flown by the Twin Otter aircraft.

vegetation cover $f(\theta)$, which is apparent from the zenith view angle θ of the thermal sensor,

$$T_{\text{RAD}}(\theta)^4 \approx f(\theta)T_c^4 + [1 - f(\theta)]T_s^4. \quad (1)$$

For a homogeneous canopy with a spherical leaf angle distribution and leaf area index F ,

$$f(\theta) = 1 - \exp\left(\frac{-0.5F}{\cos\theta}\right). \quad (2)$$

The exponential term in Eq. (2) is the “canopy gap fraction” as given by the Beer–Lambert law—the fractional area in the scene where bare soil can be viewed through gaps between individual foliar elements within the canopy.

The TSM balances the soil (subscript s) and the canopy (c) energy budgets separately, computing the system and component fluxes of net radiation ($\text{RN} = \text{RN}_c + \text{RN}_s$), sensible and latent heat ($H = H_c + H_s$) and LE ($\text{LE} = \text{LE}_c + \text{LE}_s$), and ground heat conduction (G):

$$\begin{aligned} \text{RN} &= H + \text{LE} + G \\ \text{RN}_s &= H_s + \text{LE}_s + G \\ \text{RN}_c &= H_c + \text{LE}_c. \end{aligned} \quad (3)$$

Extinction of net radiation within the canopy (RN_c) is approximated with an analytical formalism based primarily on leaf absorptivity and LAI (Campbell and Norman 1998), while G is parameterized as a fraction (0.31) of the net radiation above the soil surface (RN_s), following Choudhury et al. (1994). Canopy and soil sensible heat fluxes are computed from temperature gradients over the series resistance network in Fig. 2a:

$$\begin{aligned} H &= \rho c_p \frac{T_{\text{ac}} - T_a}{R_a} \\ H_c &= \rho c_p \frac{T_c - T_{\text{ac}}}{R_x} \\ H_s &= \rho c_p \frac{T_s - T_{\text{ac}}}{R_s}. \end{aligned} \quad (4)$$

Here, R_a is the aerodynamic resistance to turbulent transport between the canopy and the reference height, R_x is the bulk leaf boundary layer resistance, and R_s is the resistance through the boundary layer above the soil surface, while T_{ac} is the so-called momentum aerodynamic temperature (Norman and Becker 1995), T_a is the air temperature at the reference height, and ρc_p is the volumetric heat capacity of air. A modified Priest-

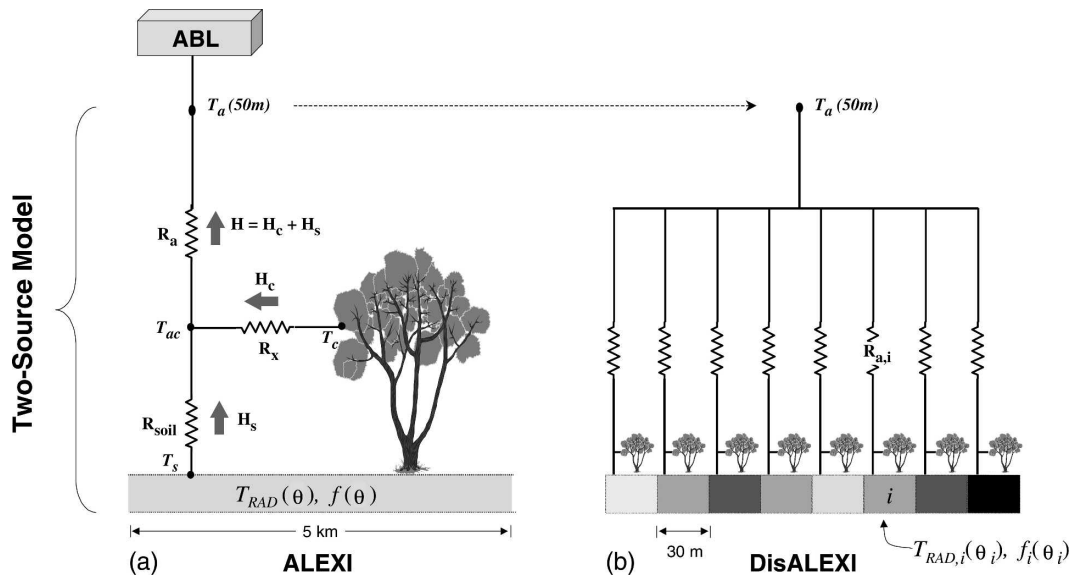


FIG. 2. Schematic diagram representing the coupled (a) ALEXI and (b) DisALEXI modeling scheme, highlighting fluxes of sensible heat (H) from the soil and canopy (subscripts c and s) along gradients in temperature (T), and regulated by transport resistances R_a (aerodynamic), R_x (bulk leaf boundary layer), and R_s (soil surface boundary layer). DisALEXI uses the air temperature predicted by ALEXI at 50 m AGL (T_a) to disaggregate 5-km ALEXI fluxes, given vegetation cover [$f(\theta)$] and directional surface radiometric temperature [$T_{RAD}(\theta)$] information derived from high-resolution remote sensing imagery at look angle θ . See Norman et al. (2003) for further details.

ley–Taylor relationship (Priestley and Taylor 1972) provides an initial estimate of canopy evapotranspiration (LE_c), and the soil evaporation rate (LE_s) is computed as a residual to the system energy budget. Details regarding the TSM algorithm are given by Norman et al. (1995), with further improvements by Kustas and Norman (1999a, 2000b).

The series model formulation in Fig. 2a assumes that soil and canopy fluxes interact; for example, sensible heat from the soil surface warms the microclimate within the canopy, thereby modifying H_c , and vice versa. Furthermore, wind and radiation penetration to soil surface (affecting R_s and R_{N_s} , respectively) are modified by the presence of an overlying canopy. This is in contrast with the patch approach, where all aspects of bare soil and vegetated patch behavior are independent (see Kustas and Norman 1999b).

b. Stress detection in the TSM

The TSM has been structured such that it will detect thermal signatures of canopy and soil moisture deficiency and reduce LE_c and LE_s accordingly. This adjustment process is demonstrated in Fig. 3, comparing flux and temperature partitioning relative to a base case with nonlimiting soil moisture. In this modeling exercise, T_{RAD} and T_a are held constant, while $f(0)$ is varied

above and below the nominal value by an amount $\Delta f(0)$. At $\Delta f(0) = 0$, the surface temperature is consistent with that expected for healthy green vegetation at the nominal cover fraction and with ample available water. For a scene with denser cover, however (moving to the right in Fig. 3), T_{RAD} is too hot; the excess temperature tends to accumulate in T_s because T_c is well regulated by the canopy transpiration rate. The soil Bowen ratio increases, as expected for a drying soil surface.

Eventually LE_s reaches 0, and, rather than allowing condensation onto the soil at midday (unlikely), LE_c is subsequently throttled back from its potential rate. Beyond this limit, the high surface temperature (relative to cover) is interpreted as being indicative of canopy stress and stomatal closure, perhaps resulting from moisture depletion in the root zone. Under ever higher canopy cover (still moving right), soil sensible heat ($H_s = RN_s - G$ at this point) starts decreasing as the available energy at the soil surface continues to diminish, and T_s stabilizes.

Physically inconsistent inputs of vegetation cover and surface temperature to the TSM can mimic this stress-induced model response. In remote sensing applications, T_{RAD} and f can become grossly incompatible as a result of image registration errors. Vegetation clumping at subpixel scales introduces a more moderate mis-

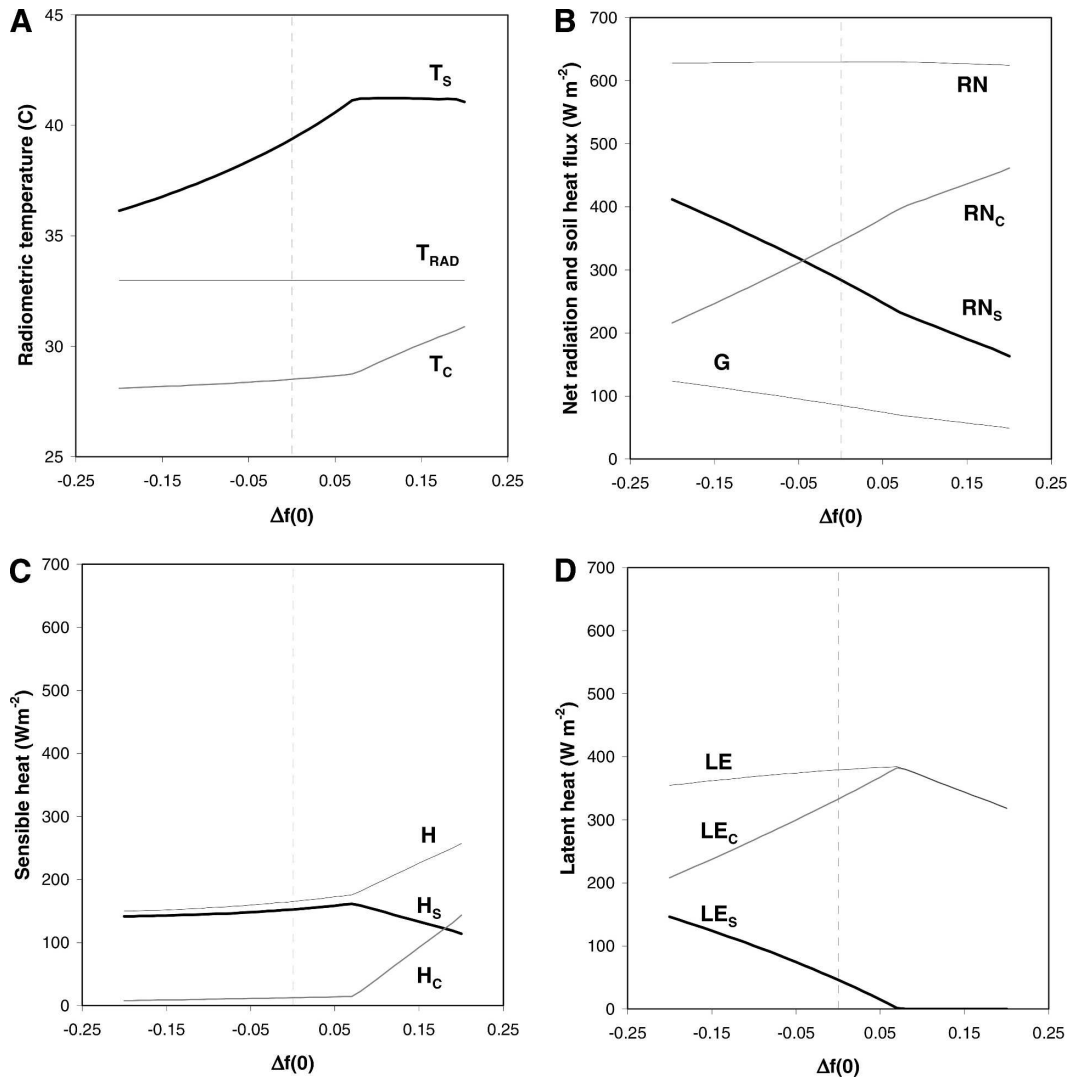


FIG. 3. Sensitivity of TSM surface flux and temperature partitioning to changes in input cover fraction for a given surface radiometric temperature (held fixed). Base case [$\Delta f(0) = 0$] represents conditions where surface temperature is consistent with healthy green vegetation at the nominal cover fraction (0.6), with nonlimiting soil moisture conditions: (a) radiometric temperature, (b) net radiation and soil heat flux, (c) sensible heat, and (d) latent heat.

match between pixel-averaged cover and temperature [$\Delta f(0) > 0$], resulting in biased flux estimates: system sensible heating will tend to be overestimated, while system latent heating is less affected (by $\sim 50\%$, see Fig. 3).

c. Remote applications: ALEXI and DisALEXI

The TSM can be applied spatially across a landscape using the mosaic approach of Koster and Suarez (1992a), provided that the upper boundary condition in air temperature (T_a) is defined at a height where conditions are relatively uniform over the modeling domain (Fig. 2b). The atmospheric “blending height” (Wiering 1986; Mason 1988) will depend on the typical

length scale of surface heterogeneity within the scene, but is generally on the order of 50–100 m, or so, above ground level (AGL). In practice, however, air temperature measurements near the blending height are not routinely available.

To extend the utility of the TSM from the field campaign trials to routine spatial analyses, a nested modeling system has been employed in which a regional-scale model provides boundary conditions for local-scale applications. For regional-scale flux mapping, the TSM has been coupled with a simple model of ABL development (McNaughton and Spriggs 1986), so that the air temperature at the blending height is simulated and consistent with the modeled surface fluxes (Fig. 2a).

This coupled model is referred to as the Atmosphere–Land Exchange Inverse (ALEXI) model (Anderson et al. 1997). The lower boundary conditions for ALEXI are provided by TIR observations taken at two times during the morning (1.5 and 5.5 h after local sunrise) from a geostationary platform, such as GOES. The ABL model relates the rise in air temperature at the blending height during this interval, and the resulting growth of the ABL, to the time-integrated influx of sensible heating from the surface.

In the Disaggregated ALEXI (DisALEXI) algorithm (Norman et al. 2003; Anderson et al. 2004b), the air temperature field predicted by ALEXI at the second GOES observation time (t_2) is used to disaggregate the GOES-scale fluxes (5–10-km resolution) to finer spatial scales (Fig. 2b). The ALEXI-derived values of T_a serve as upper boundary conditions, while the TSM is applied to high-resolution (15 m–1 km) temperature and cover data from satellites like Landsat, Advanced Spaceborne Thermal Emission and Reflection Radiometer (ASTER), or Moderate Resolution Imaging Spectroradiometer (MODIS) that are collected over the same scene. To evaluate model performance, the resulting high-resolution flux predictions can be reaggregated using a source footprint–weighting scheme and compared directly with tower or aircraft observations. Good agreement at the footprint scale also provides indirect validation of the aggregate 5-km ALEXI fluxes, which are otherwise difficult to assess quantitatively.

3. Characterizing vegetation clumping

Equation (2) holds for homogeneous canopies where the vegetation cover is relatively uniform across the model grid cell area. To accommodate the nonrandom leaf area distributions characteristic of agricultural and other heterogeneous landscapes, the LAI in Eq. (2) can be modified by a clumping index Ω ,

$$f(\theta) = 1 - \exp\left(\frac{-0.5\Omega F}{\cos\theta}\right) \quad (5)$$

(e.g., Nilson 1971; Chen and Black 1992; Chen and Cihlar 1995; Kucharik et al. 1999). Lower values of Ω indicate stronger clumping, while $\Omega = 1$ for a homogeneous canopy with a random dispersion of leaf area, and $\Omega > 1$ indicates more regularized distributions.

The apparent clumping index will typically vary with view zenith angle θ (Chen 1996; Kucharik et al. 1997; Kucharik et al. 1999), attaining a minimum value at nadir view (Ω_0), and increasing toward some maximum value (Ω_{\max}) at more oblique angles as the gaps between the foliage elements become obscured. In the case of row crops and other stands with anisotropic

distributions, apparent clumping may also vary with view azimuth angle ϕ .

a. Small-scale (subpixel) clumping

Prior to closure, a row crop canopy can be thought of conceptually as being a series of parallel tubes of vegetation, each of characteristic width w and height h , and separated by the row spacing r . Of the total area within an idealized field, a fraction $f_{\text{veg}} = w/r$ will have some canopy cover, and $1 - f_{\text{veg}}$ will be totally bare. For a field with $f_{\text{veg}} = 1/4$ and an areally averaged LAI (\bar{F}) of 1, the local LAI within the row will be $F_L = \bar{F}/f_{\text{veg}} = 4$.

The total fraction of the scene occupied by soil (f_{soil}), as viewed from overhead ($\theta = 0$), is the sum of the fractional bare area between the rows ($1 - f_{\text{veg}}$) and the area where soil is seen through gaps in the canopy (f_{gap}),

$$f_{\text{soil}}(0) = (1 - f_{\text{veg}}) + f_{\text{veg}}f_{\text{gap}} \equiv \exp\left[\frac{-0.5\Omega_0\bar{F}}{\cos(0)}\right], \quad (6)$$

where

$$f_{\text{gap}} = \exp\left[\frac{-0.5F_L}{\cos(0)}\right], \quad (7)$$

again assuming a spherical leaf angle distribution. The clumping index is the value that corrects Beer's law at the pixel scale [right-hand side of Eq. (6)] to provide for the proper accounting of f_{soil} . Solving Eqs. (6)–(7) for the clumping index gives $\Omega_0 = 0.49$ for the hypothetical field described above. Approximate functional relationships describing the dependence of clumping index on view zenith and azimuth angles [$\Omega(\theta, \phi)$] for corn and soybean row crops are given in the appendix.

b. Upscaling clumping indices

At scales exceeding the average plot size, the effective clumping index in agricultural settings will additionally reflect field-to-field contrasts in LAI. This component will be independent of the view angle because the effective scale of variation is much larger than the vegetation height.

In this study, a bulk clumping index $\Omega_G(\theta_G, \phi_G)$, representative of the 5-km scale and view angle of a GOES thermal pixel, is estimated by aggregating nadir-looking Landsat data at 30-m resolution. The process is as follows:

- 1) Nadir view clumping at the sub-Landsat-pixel scale (i.e., row-scale clumping) is estimated for corn and soybean sampling sites as described in the preceding section. These values depend on measurements of

fractional row coverage (f_{veg}) and average LAI (\bar{F}) made in the field. Subpixel clumping at nadir view is denoted as $\Omega_s(0, 0)$.

- 2) Subpixel clumping values are corrected via Eqs. (A1)–(A4) to the GOES view angle, giving values of $\Omega_s(\theta_G, \phi_G)$ for each sampled corn- and soybean fields. These angular corrections do not involve any additional in-field measurements (see the appendix).
- 3) A typical subpixel clumping index for corn and soybean is determined for each field-sampling date by averaging over all fields of a given crop type.
- 4) A bulk clumping index is computed for each 5-km GOES tile covering the Walnut Creek watershed in a manner analogous to Eqs. (6)–(7). A given 5-km tile contains N_{tot} 30-m Landsat cells, each of which can be assigned an areally averaged value of LAI based on observed vegetation indices. Of these N_{tot} cells, N_v are found to contain nonzero LAI, and $1 - N_v$ are completely bare at the 30-m scale. For each tile then, f_{veg} is computed as N_v/N_{tot} , while \bar{F} is the tile-averaged LAI ($\sum_i \bar{F}_i/N_{\text{tot}}$), and \bar{F}_i is the average LAI in the i th cell. Then,

$$f_{\text{soil}}(\theta_G, \phi_G) = (1 - f_{\text{veg}}) + f_{\text{veg}} \bar{f}_{\text{gap}} \\ \equiv \exp \left[\frac{-0.5 \Omega_G(\theta_G, \phi_G) \bar{F}}{\cos \theta_G} \right], \quad (9)$$

where

$$\bar{f}_{\text{gap}} = \frac{1}{N_v} \sum_{i=1}^{N_v} \exp \left[\frac{-0.5 \Omega_{s,i}(\theta_G, \phi_G) \bar{F}_i}{\cos \theta_G} \right]. \quad (10)$$

In Eq. (10), the gap fraction in each i th Landsat cell is augmented by an estimate of subpixel clumping $\Omega_{s,i}(\theta_G, \phi_G)$, set to the nominal corn or soybean value determined in step 3 (or other nominal value) based on a 30-m land cover classification map. Completely bare fields (preemergence or fallow) are accounted for in the $(1 - f_{\text{veg}})$ term.

c. Incorporating effects of clumping into the TSM

The clumping index modifies several terms within the TSM (and ALEXI/DisALEXI) system of equations (Kustas and Norman 1999a, 2000b). Clumping at the view zenith angle of the thermal sensor reduces the effective leaf area in Eq. (2), affecting the partitioning of radiometric temperature and surface fluxes between the soil and canopy. An analogous clumping index at the solar zenith angle is included in canopy radiative transfer equations, augmenting both RN_s and G . We also consider effects on wind speed inside the clumped canopy and above the soil surface, and the associated

heat transfer resistances. Kustas and Norman (2000b) describe how Ω_0 modifies the in-canopy wind profile coefficients of Goudriaan (1977), serving to increase R_x and decrease R_s , and altering the partitioning of system sensible heating. The clumping index, therefore, provides some degree of decoupling between large-scale vegetated and bare patches, as would be expected.

4. Data

a. Field measurements

The SMACEX component of SMEX02 was conducted from mid-June to mid-July 2002 within a 20 km \times 40 km area, including the Walnut Creek watershed (Fig. 1). Within the WC study area, 21 corn- and 10 soybean fields were selected as sites for intensive vegetation sampling. Sampling occurred in four rounds and included measurements of LAI, stand density, canopy height, and row width and spacing. LAI data were acquired with LAI-2000 Plant Canopy Analyzer (LICOR Inc., Lincoln, Nebraska) units, programmed to sample the average LAI across the entire row width. Field-averaged values of vegetation cover fraction varied from 0 to 1 over the course of the experiment, with large site-to-site variability (Fig. 4). See Anderson et al. (2004a) for more detail regarding the SMEX02 vegetation datasets.

b. Satellite data

Throughout SMACEX, multiband imagery, acquired with the GOES, *Landsat-5 (L5)*, and *Landsat-7 (L7)* satellites, were collected and archived. Days with clear morning skies (required by ALEXI) occurred on day of year (DOY) 167, 174, 178, 179, 181, 182, and 183 (later dates were affected by smoke from western wildfires; Walthall et al. 2004). Landsat overpasses with clear views of the WC study area occurred on DOY 174 (*L5*), 182 (*L7*), and 189 (*L7*). Therefore, flux disaggregation with DisALEXI could be performed for DOY 174 and 182.

1) SURFACE RADIOMETRIC TEMPERATURE

The coarse-resolution brightness temperature maps used in ALEXI were obtained with the *GOES-8* imager within the 10.2–11.2- μm (band 4) window. Thermal data are available every 15 min at an average zenith-viewing angle of approximately 52°, in azimuth looking 27°W of north, and at a nominal spatial resolution of 5 km at the location of the SMEX02 study area. Atmospheric corrections (French et al. 2003) were performed using standard observations from the national radio-

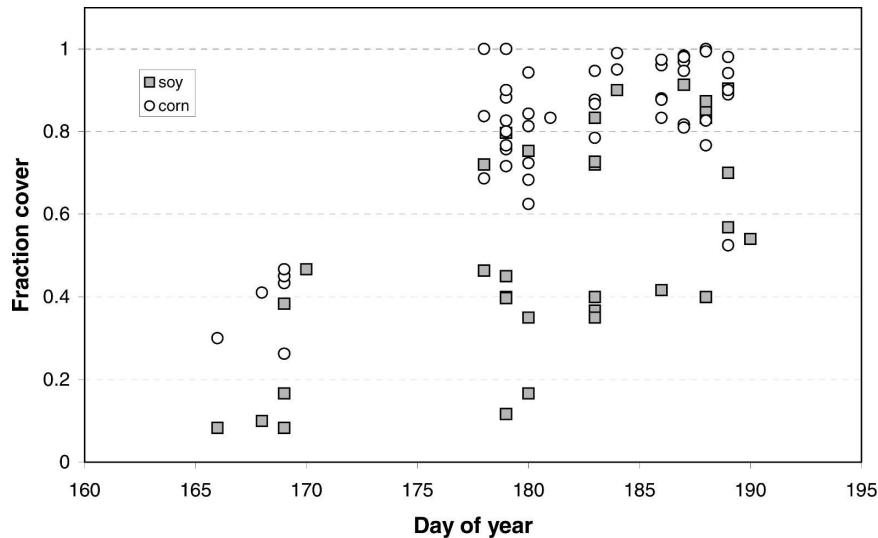


FIG. 4. Average vegetation cover fraction $f(0)$ measured at each WC site as a function of sampling date.

sonde network and a vegetation cover–dependent correction for surface emissivity (Mecikalski et al. 1999).

The Landsat TIR data used in the disaggregation were extracted from band 6 imagery, which is acquired at 120-m spatial resolution on *L5* (DOY 174) and 60-m resolution on *L7* (DOY 182). The original level 1G Thematic Mapper (TM) data were georegistered with respect to road intersections, then atmospherically corrected with the Moderate Spectral Resolution Atmospheric Transmittance (MODTRAN) radiative transfer model (Berk et al. 1998), using radiosonde data and default aerosol profiles and adjusted for surface emissivity variations (see Li et al. 2004 for further details).

2) VEGETATION COVER

Coarse-scale estimates of fractional vegetation cover $f(0)$ and cell-averaged LAI [from Eq. (2)] used in ALEXI were derived from a biweekly composited Normalized Difference Vegetation Index (NDVI) product generated with the Advanced Very High Resolution Radiometer (AVHRR) at 1-km resolution (Eidenshink 1992). These NDVI values were scaled with

$$\text{NDVI}^* = \frac{\text{NDVI} - \text{NDVI}_{\min}}{\text{NDVI}_{\max} - \text{NDVI}_{\min}}; \quad f(0) = (\text{NDVI}^*)^2 \quad (11)$$

(Gillies and Carlson 1995), which reduces sensitivity to atmospheric effects and AVHRR view angle. The scaling limits NDVI_{\min} and NDVI_{\max} were selected as the lower and upper 3% tails of the frequency distribution

of all NDVI values measured over the United States from March to August, excluding pixels that were classified as water. The 1-km cover estimates were then linearly averaged to the 5-km ALEXI grid. To obtain LAI fields for arbitrary modeling dates, the two bracketing AVHRR composites were interpolated from their biweekly midpoints.

For the disaggregation, LAI was retrieved from the Normalized Difference Water Index (NDWI), $\text{NDWI} = (\text{NIR} - \text{SWIR})/(\text{NIR} + \text{SWIR})$ (Gao 1996), computed using 30-m resolution (on both *L5* and *L7*) imagery from TM bands 4 (NIR) and 5 [shortwave infrared (SWIR)]. The retrieval relationship was developed empirically by Anderson et al. (2004a) in comparison with the in situ measurements of row-averaged LAI, and yields a root-mean-square difference (rmsd) of 0.66 with minimal bias (Fig. 5a). Anderson et al. (2004a) found that NDWI saturated at higher levels of vegetation cover than did NDVI, allowing for the better characterization of LAI at high resolution under full-canopy conditions.

The dense spatial distribution of ground observations collected during SMACEX provides a unique opportunity for the stepwise validation of remote LAI retrieval up to the 5-km scale. The 30-m estimates of \bar{F} based on TM NDWI (validated directly with respect to ground data; Fig. 5a) were averaged to the 5-km scale for comparison with AVHRR-based estimates over the WC domain, yielding a rmsd of 0.23 and a bias of 0.03 (Fig. 5b). This upscaling exercise suggests that Eq. (11) is giving a reasonable representation of cell-averaged LAI at the 5-km scale, which will be important in es-

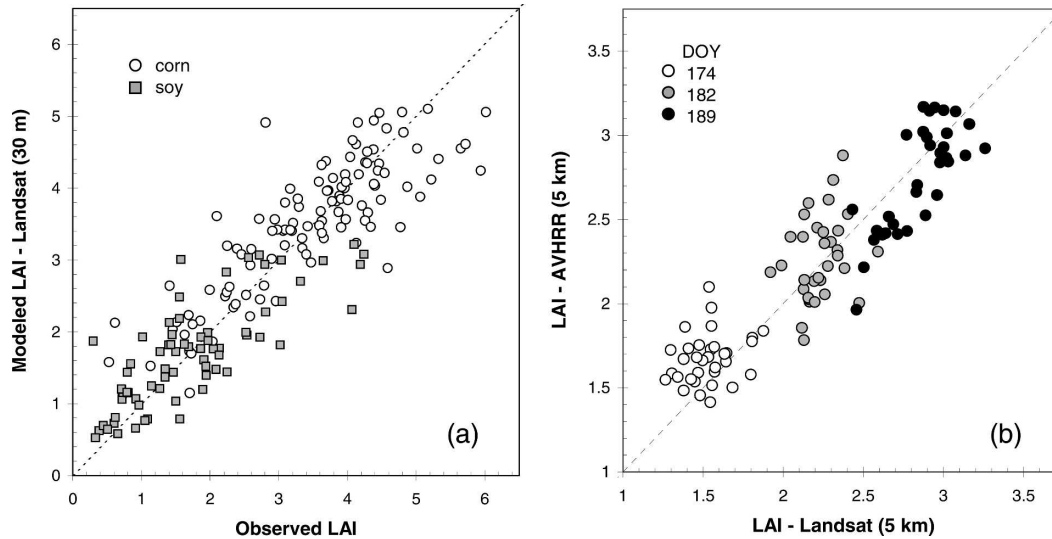


FIG. 5. Comparison of (a) LAI measured in situ at sampling locations during SMACEX with values retrieved from Landsat NDWI at 30-m resolution and (b) LAI retrieved from Landsat NDWI and AVHRR NDVI on DOY 174, 182, and 189, both aggregated to 5-km resolution.

tablishing the need for including clumping effects in the regional model.

3) LAND COVER CHARACTERISTICS

At both coarse and finescales, satellite-derived fractional cover estimates have been used in conjunction with a gridded land surface classification to assign relevant surface parameters, such as roughness and radiometric properties (see Mecikalski et al. 1999). Coarse-scale assessments for ALEXI were based on the University of Maryland (UMD) 1-km Global Land Cover Product (Hansen et al. 2000).

To define surface parameters for DisALEXI, we used a supervised classification at 30-m resolution developed by Doraiswamy et al. (2004), based on multi-temporal Landsat imagery. Within the watershed, corn and soybean occupied 86% of the total area, with an additional 7% that were roads, 4% grass, 2% trees, and trace proportions of pixels classified as being urban and alfalfa. Of the total area covered, corn occupied 48% and soybean 52%.

c. Ancillary meteorological inputs

Ancillary atmospheric data required by the modeling system include an estimate of wind speed (50 m AGL) and an early morning atmospheric temperature profile at each 5-km grid cell in the ALEXI domain. These input fields are currently created with the analysis component of a mesoscale model (in initialization mode) using standard observations from the synoptic weather

and radiosonde networks. Downwelling solar and long-wave radiation estimates were extracted from hourly GOES-based products at 5-km resolution (Diak et al. 1996; Diak et al. 2000; Otkin et al. 2005). DisALEXI was assigned meteorological inputs from the nearest ALEXI grid cell.

d. Tower data

The EC data used here for validation were acquired at 10 towers in the WC watershed (see Fig. 1). Of these, five towers were located in cornfields, and five in soybean fields, which is proportionally representative of the general cropping census within the WC area. Each tower made measurements of sensible, latent, and soil heat flux, soil temperature and moisture for the 0–6-cm layer, net radiation, air temperature, wind speed and direction, relative humidity, and radiometric surface temperature. For more details regarding the SMACEX EC and supporting data, see Prueger et al. (2005).

e. Aircraft data

From 15 June to 6 July, the Twin Otter aircraft of the Canadian National Research Council flew several missions over the WC study area on transects designed to intersect many of the EC towers. Turbulent fluxes of heat, water, CO₂, ozone, and momentum were measured at an altitude of approximately 40 m on repeated passes over six tracks ranging in length from 6 to 12 km (Fig. 1). Details of the aircraft-based measurements are given by MacPherson and Wolde (2002) and MacPherson et al. (2003).

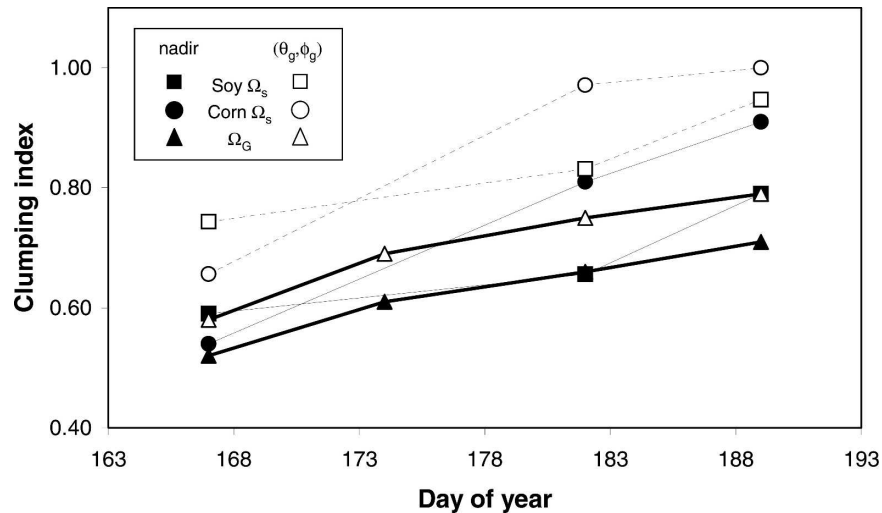


FIG. 6. Apparent clumping index at nadir view ($\theta = \phi = 0$) and at the GOES view angle ($\theta = 52^\circ$, $\phi = 27^\circ$ west of north) as a function of date, at sub-30-m scales for corn and soybean (Ω_s), and at the 5-km scale (Ω_G).

In addition, high spatial resolution visible, NIR, and thermal imagery were collected periodically over the WC area with the Utah State University (USU) airborne digital imaging system (Neale and Crowther 1994). In this study, USU imagery collected on DOY 167 were used to generate a high-resolution map of LAI, supplementing Landsat-derived maps on DOY 174, 182, and 189 (see Anderson et al. 2004a for further information).

5. Results and discussion

a. Vegetation clumping

Using ground-based measurements of row-averaged LAI and fractional row coverage (f_{veg}) in Eqs. (6)–(7), row-scale clumping indices at nadir view were developed around DOY 167, 182, and 189. These dates coincide with the available high-resolution aircraft/Landsat LAI images (there was no vegetation sampling around DOY 174). The time evolution in the average $\Omega_s(0, 0)$ for developing corn- and soybean fields is shown in Fig. 6. Mean values range between 0.5 and 0.9, with soybean generally showing stronger clumping (lower Ω_s), except near the beginning of the experiment when the LAI in soybean was very low. Theoretically, the clumping index should approach unity in the limits of $\bar{F} = 0$ and large \bar{F} .

The sub-30-m clumping indices at nadir view were adjusted to the GOES zenith and azimuth view angles (52° and 27° W of north, respectively) using Eqs. (A1)–(A4) (also plotted in Fig. 6). Corn and soybean row orientations in the WC area were east–west and north–south in

approximately even proportions. Therefore, values of Ω_s at $\phi = 27^\circ$ and $90^\circ - 27^\circ = 63^\circ$ have been averaged to represent a mean watershed value. Figure 6 indicates that row-clumping effects are less important at the GOES view angle than at nadir, as expected.

To obtain estimates of clumping at the scale of the GOES pixel (Ω_G), Landsat and aircraft LAI data on DOY 167, 174, 182, and 189 were aggregated over 5-km tiles using Eqs. (8)–(9), assuming subpixel clumping indices for corn and soybean as described above (with interpolated values for DOY 174). For comparison, Ω_G was determined both at nadir and at the GOES view angle. Landsat pixels assigned to the road and urban classes were assumed to have subpixel clumping of 0.5; all other classes were assumed to have clumping of 0.9 at nadir and 1.0 at $\theta_G = 52^\circ$. The 5-km estimates include clumping on the field scale, and, therefore, approach asymptotic limits that are smaller than the sub-30-m values (Fig. 6). Over the course of SMACEX, nadir view clumping at the watershed scale varied between 0.5 and 0.7.

b. ALEXI

To study the effects of vegetation clumping on coarse-scale model fluxes, ALEXI simulations at 5-km resolution were generated for seven clear mornings during SMACEX assuming cases A: no vegetation clumping, B: the “observed” 5-km clumping factor at the GOES view angle, and C: clumping as would be observed at nadir. Model flux components have been spatially averaged over the WC domain for comparison with average tower and aircraft fluxes acquired around

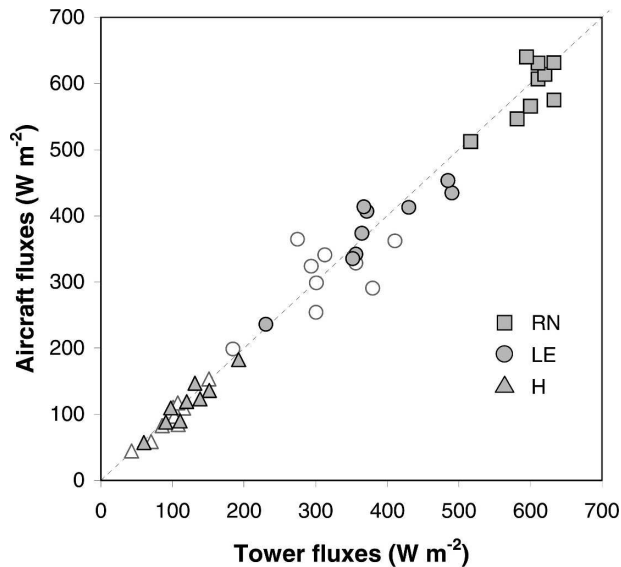


FIG. 7. Comparison of spatially averaged tower and aircraft flux measurements on several days during SMACEX, acquired around the ALEXI modeling time t_2 (~ 1045 LST). Open H and LE symbols indicate uncorrected measurements, while gray-filled symbols represent fluxes corrected for energy budget closure by conserving the Bowen ratio.

the modeling time, $t_2 \sim 1045$ LST. Cells containing the city of Ames were excluded from the average, because urban fluxes are not represented in the observational datasets.

Comparisons between EC flux measurements and model predictions are often complicated by a lack of “closure” in the observed energy budget; typically, $RN - G > H + LE$ in EC datasets (Twine et al. 2000; Wilson et al. 2002), while models inherently enforce closure. To demonstrate the magnitude of this uncertainty, we quote tower and aircraft H and LE fluxes both as measured (unclosed) and with an energy budget closure correction (closed) preserving the observed Bowen ratio (Twine et al. 2000). The average G measured at the EC tower sites has been used to close both the tower and aircraft budgets.

The spatially averaged tower and aircraft EC fluxes agree very well (Fig. 7), suggesting that these measurement sets are reasonably representative of the actual watershed-scale surface fluxes, and giving a measure of observational uncertainty at this scale. When the unclosed fluxes are compared, there is proportionally greater scatter in the latent heat flux measurements (50 W m^{-2} or $\sim 16\%$ of the average tower LE flux) than in those of sensible heat (10 W m^{-2} or $\sim 10\%$). However, enforcing closure in both datasets equalizes the proportional scatter, reducing the rmsd in LE to 30 W m^{-2} (8% of the average closed LE), as shown in Fig. 7.

Day-to-day variations in model energy budget com-

ponents at time t_2 are compared with the tower and aircraft measurements in Fig. 8, with scatterplot comparisons in Fig. 9 and related statistics in Table 1. Included in Table 1 is the coefficient of efficiency (E) that was proposed by Nash and Sutcliffe (1970) as a performance metric preferable to the coefficient of determination (r^2), which can indicate perfect agreement even in the presence of systematic model biases. The aircraft and tower data in Fig. 8 agree well, showing a secular decrease in Bowen ratio as the crops mature. When clumping is neglected, ALEXI significantly overestimates the sensible heat flux on DOY 174 and 178. At this time, the average fractional cover in area corn- and soybean fields was passing through the transitional zone of ~ 0.4 – 0.6 (Fig. 4), where clumping effects are most problematic from a modeling standpoint (Kustas and Norman 2000a). Model values of latent heat are generally bounded by the closed and unclosed tower and aircraft fluxes, while the soil heat flux is underestimated early in the experiment.

When clumping predicted at the GOES view angle is included, the ALEXI sensible heat estimates are substantially improved and G is increased as more net radiation penetrates to the soil surface. Agreement in H and LE is further improved by using the clumping indices determined for a nadir view angle. This would indicate that either the 5-km-scale clumping index is being slightly overestimated by our techniques (or there is some other bias in the model), or that the spatially continuous ALEXI model is picking up some higher sensible heating areas that are not being sampled by either the tower network or the aircraft transects. For cases B and C above, the rmsd in latent heat predictions of 34 W m^{-2} approach the rmsd between the aircraft and tower flux measurements after closure correction (30 W m^{-2}), although the modeled sensible heat shows larger scatter (17 – 22 W m^{-2}) relative to the measurement intercomparison (10 W m^{-2}).

It could be questioned whether the simple model parameterization of G ($0.31 RN_s$) might be to blame for the problems associated with H , without needing to invoke any issues of clumping. This does not appear to be the case. In the TSM, errors in G are generally absorbed into estimates of LE rather than H because H is well constrained by the surface temperature data, while the soil evaporation component of LE is determined purely as a residual. Here, the error is clearly in H , with a counterbalancing error of the opposite sign in G fortuitously yielding an adequate prediction of LE . Clumping simultaneously solves problems with both H and G , and seems the simplest possible explanation.

The flux observation datasets from SMACEX were sufficiently dense (multiple towers per model grid cell)

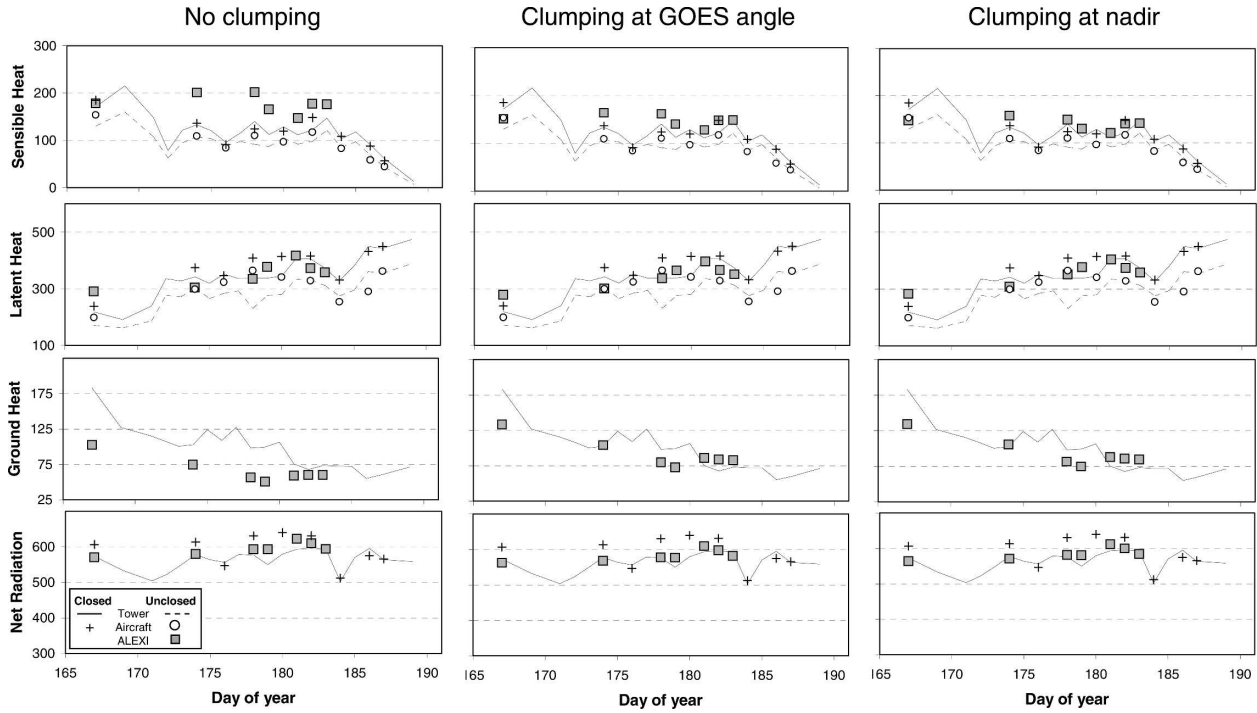


FIG. 8. Time evolution of tower and aircraft flux component measurements compared with predictions from the ALEXI model for clumping cases (left) A, (middle) B, and (right) C, each averaged over the WC study area. Tower and aircraft data are shown both as unclosed (raw) and with an energy budget closure correction.

and spatially representative of average surface flux conditions at the watershed scale to warrant a direct comparison with ALEXI output. In contrast, Anderson et al. (2004b) compared 5-km ALEXI flux estimates with closure-corrected fluxes from the Oklahoma Mesonet—a sparser network with only one EC tower per ALEXI cell—and obtained significantly larger rmsd values of 92 and 60 $W m^{-2}$ for H and LE , respectively.

The scatter in this case was strongly affected by local surface heterogeneity around individual tower sites and did not reflect the true accuracy of the modeled fluxes. This is evidenced by the fact that agreement with Mesonet flux measurements was significantly improved (to 30–35 $W m^{-2}$ rmsd) when the modeled 5-km fluxes were disaggregated down to the scale of the tower footprint (Anderson et al. 2004b).

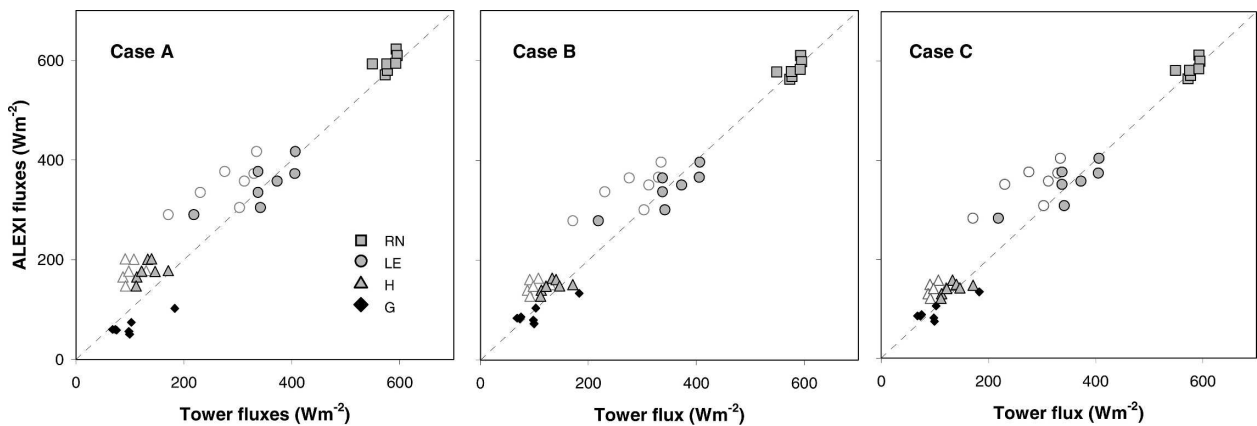


FIG. 9. Comparison of tower flux measurements with model predictions from the ALEXI model for clumping cases (left) A, (middle) B, and (right) C, averaged over the WC study area. Open H and LE symbols indicate uncorrected measurements, while gray-filled symbols represent fluxes corrected for energy budget closure by conserving the Bowen ratio.

TABLE 1. Quantitative measures of ALEXI model performance in estimating WC-averaged tower fluxes.*

Flux	<i>N</i>	\bar{O}	MBE	rmsd	r^2	<i>E</i>	Percent error
		(W m ⁻²)	(W m ⁻²)	(W m ⁻²)			
Case A							
RN	7	580	15	21	0.26	-1.02	3
LE	7	346	5	37	0.62	0.61	9
<i>H</i>	7	134	44	48	0.20	-5.05	33
<i>G</i>	7	100	-34	41	0.76	-0.29	34
All	28	290	7	38	0.97	0.96	11
Case B							
RN	7	580	2	14	0.35	0.15	2
LE	7	346	-4	34	0.71	0.66	8
<i>H</i>	7	134	15	22	0.27	-0.30	15
<i>G</i>	7	100	-8	24	0.72	0.57	19
All	28	290	1	25	0.98	0.98	7
Case C							
RN	7	580	5	15	0.32	0.00	2
LE	7	346	4	34	0.70	0.66	8
<i>H</i>	7	134	7	17	0.39	0.25	12
<i>G</i>	7	100	-7	24	0.72	0.58	19
All	28	290	3	24	0.99	0.99	6

* Here *N* is the number of observations, \bar{O} is the mean observed flux, MBE is the mean bias error ($\bar{P} - \bar{O}$), rmsd is the root-mean-square difference between the modeled (*P*) and observed (*O*) quantities, r^2 is the coefficient of determination in a linear regression of *P* on *O*, *E* is the coefficient of efficiency, and the percent error is defined as the mean absolute difference between *P* and *O* divided by the mean observed flux

c. DisALEXI

Using air temperature predictions at the blending height from ALEXI for the three clumping cases discussed above, 5-km flux predictions over the WC wa-

tershed were disaggregated to the 120-m scale (*L5* thermal resolution) on DOY 174, and to 60 m (*L7*) on DOY 182. Nadir values of row-scale clumping were used in DisALEXI because the Landsat view was from approximately overhead. For cases B and C, clumping indices were assigned according to the modeling date and pixel land class. For case A, subpixel clumping was set to 1 for all land classes.

To correct for residual biases between the fine- and coarse-scale thermal remote sensing data (resulting from sensor calibration, atmospheric correction, etc.), the Landsat radiometric temperature fields have been adjusted with a constant offset chosen such that the bias between reaggregated sensible heat fluxes and ALEXI predictions of *H* is minimized, on average, across the WC area. Derived offsets ranged in magnitude between 0.5° and 1.5°C. Employing this temperature normalization technique, DisALEXI flux estimates are compared in Fig. 10 and Table 2 with tower measurements at time *t*₂ on both days. The disaggregated flux values reported here are weighted averages over the tower footprint, as estimated with a stability-corrected version of the one-dimensional analytical model of Schuepp et al. (1990, 1992). As with ALEXI, agreement with tower fluxes is significantly improved when clumping is considered, particularly for sensible and latent heating. The rmsd errors in *H* and LE of 30–40 W m⁻² for cases B and C are comparable to those obtained with DisALEXI over generally less complex landscapes in Oklahoma, on the order of 30–35 W m⁻² (Anderson et al. 2004b).

The partitioning of the total latent heat flux by ALEXI/DisALEXI (case C) between the soil and canopy on DOY 174 and 182 is shown in Fig. 11, and is qualitatively reasonable. The disaggregated fluxes

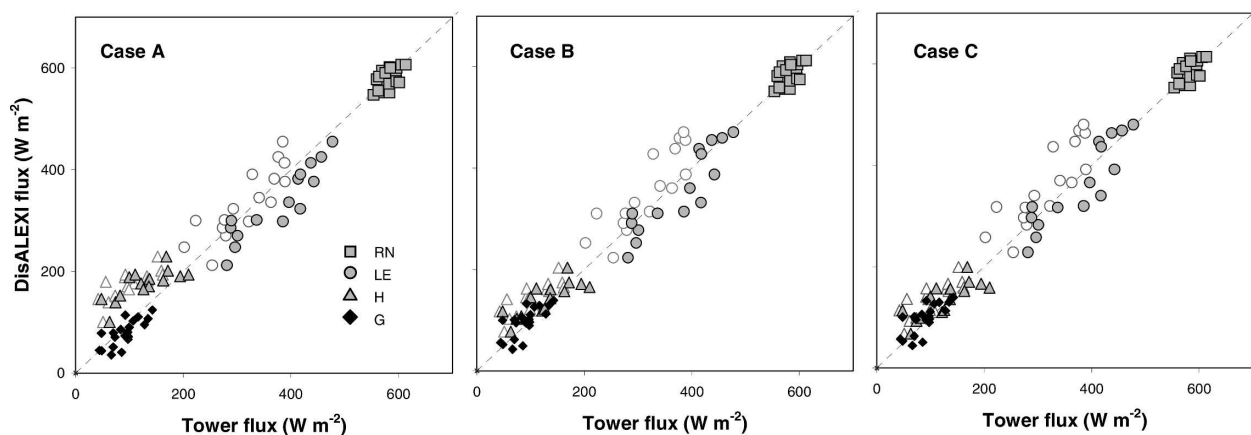


FIG. 10. Comparison of tower flux measurements with model predictions from the DisALEXI model for clumping cases (left) A, (middle) B, and (right) C, reaggregated over the tower footprint. Open *H* and LE symbols indicate uncorrected measurements, while gray-filled symbols represent fluxes corrected for energy budget closure by conserving the Bowen ratio.

TABLE 2. Quantitative measures of DisALEXI model performance in estimating fluxes measured at individual EC towers in the WC study area; N , \bar{O} , MBE, rmsd, r^2 , E , and percent error are the same as in Table 1.

Flux	N	\bar{O} (W m^{-2})	MBE (W m^{-2})	rmsd (W m^{-2})	r^2	E	Percent error
Case A							
RN	19	582	-2	17	0.31	-0.06	2
LE	15	376	-42	50	0.83	0.44	11
H	15	127	48	56	0.57	-0.47	39
G	20	86	-8	23	0.68	0.62	23
All	69	295	-2	38	0.97	0.97	10
Case B							
RN	19	582	2	17	0.29	-0.04	2
LE	15	376	-22	41	0.81	0.61	9
H	15	127	15	32	0.63	0.52	20
G	20	86	10	25	0.63	0.61	23
All	69	295	2	29	0.98	0.98	8
Case C							
RN	19	582	4	18	0.30	-0.18	2
LE	15	376	-15	38	0.81	0.67	9
H	15	127	9	30	0.61	0.57	19
G	20	86	11	25	0.63	0.54	23
All	69	295	3	28	0.98	0.98	7

within the WC study area reflect the regional behavior that is predicted by ALEXI—canopy transpiration increases as the cornbelt greens up, while soil evaporation decreases to low levels by 1 July as a result of an extended dry down that encompassed much of the Midwest. Ground-based measurements made in the watershed during SMEX02 confirm a secular decrease in near-surface soil moisture during this interval (Jackson et al. 2003). When clumping is neglected, the temporal behavior is qualitatively similar to that shown in Fig. 11, although the partitioning shifts more of the latent heat flux to the canopy component.

d. Evaluation of the modeling approach

The propriety of applying the series resistance representation in Fig. 2a to a strongly clumped canopy could be called into question. For clumping at row scales (as in the DisALEXI evaluations), the canopy does influence conditions at the soil surface between the rows, and the series model is appropriate. Kustas and Norman (1999a, 2000b) also obtained good results in applying the clumped series version of the TSM to cotton row crops.

The field-scale organization incorporated into the 5-km clumping estimates used in ALEXI is more problematic. Strictly speaking, the series model assumes that the microclimate (T_{ac}) inside a field with full-canopy

cover also prevails above the bare soil in a neighboring fallow field. While this is obviously not the case, resulting errors in representation appear to be offsetting on the watershed scale, yielding good comparison with tower and aircraft flux measurements. The fact that the ALEXI flux disaggregation process (which treats vegetated and bare fields as independent patches) is giving good agreement at the tower footprint scale is further proof that the 5-km flux estimates are reasonable.

These results suggest that this economical approach to accounting for heterogeneity in the TSM works well over the agricultural landscape studied here, with the advantage for large-scale applications being that the same equations can be applied to both clumped and homogeneous canopies. The extreme contrast in conditions that is present within the WC study area near the beginning of the experiment [$\Omega_G(0, 0) \sim 0.5$] provides a good test of this modeling framework. Future evaluations will be conducted over clumped landscapes in more arid regions.

e. Implications for routine flux modeling

As demonstrated above, the nonuniform distribution of vegetation across the landscape at subgrid scales can affect TSM flux predictions during periods when spatial contrasts in vegetation cover are strong. In the row crops studied here, clumping appears to be problematic for a relatively short portion of the growing season as the scene-averaged cover fraction passes through 0.5. This is likely an issue that is common to most thermal-based remote sensing algorithms that require consistent temperature and vegetation cover inputs. A methodology for assessing vegetation clumping at many scales using routine satellite data will, therefore, be of great benefit.

Lacaze et al. (2002), Roujean and Lacaze (2002), and Chen et al. (2003) describe methods for retrieving clumping indices from the land surface bidirectional reflectance distribution function (BRDF) as measured by airborne and spaceborne Polarization and Directionality of Earth Radiation (POLDER) instruments. These same techniques have also been applied to MODIS BRDF products (J.-L. Roujean 2004, personal communication). This approach has the advantage that it does not require subpixel information; the subpixel canopy structure is inferred by looking at the canopy from multiple view angles, rather than at higher spatial resolution. Maps of MODIS-derived clumping index are being assessed in comparison with the detailed ground- and Landsat-based measurements described here, and with data collected in other biomes around the world. Preliminary results from these comparisons are encouraging and will be conveyed in upcoming publications.

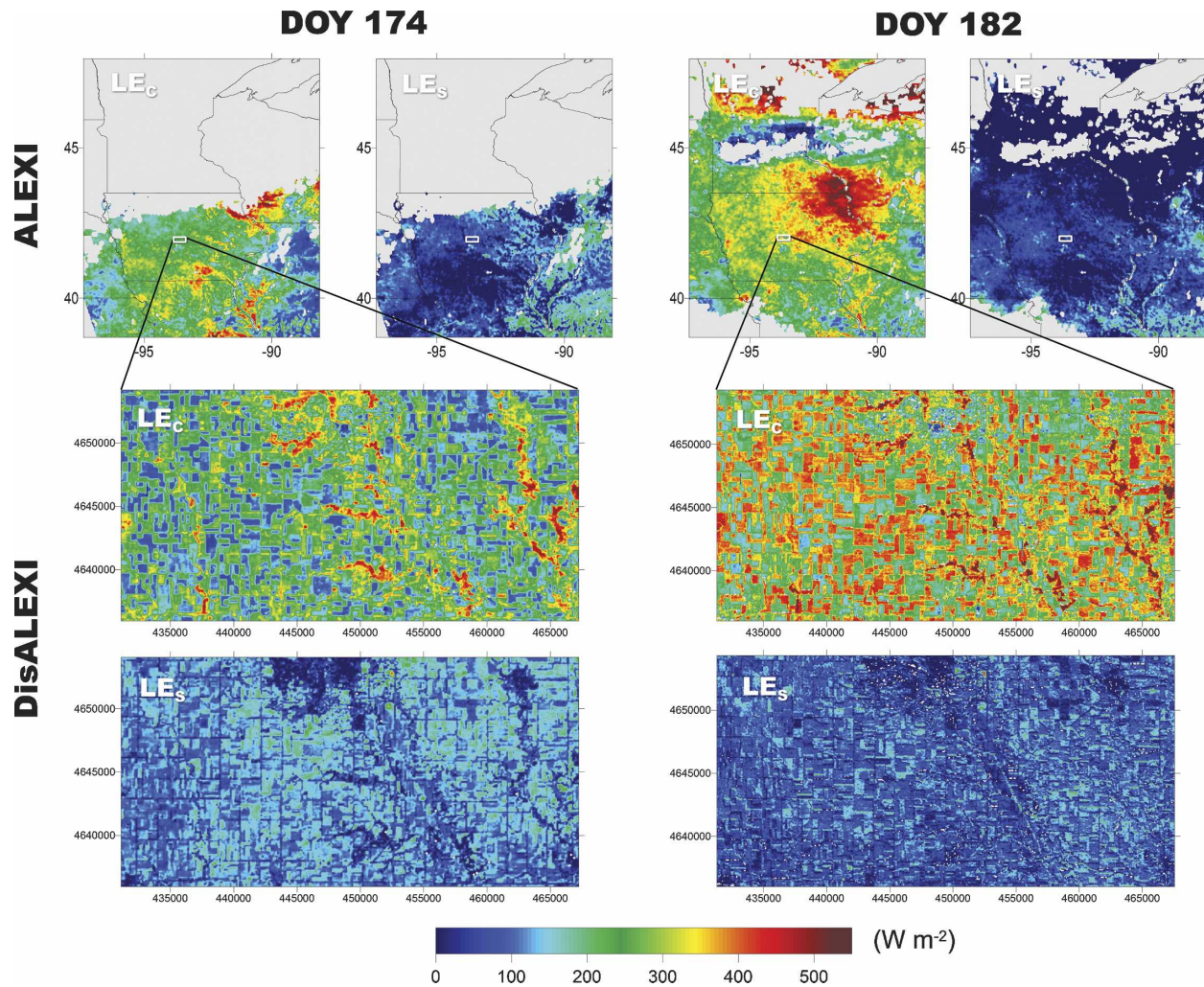


FIG. 11. Maps of canopy transpiration (LE_c) and soil evaporation (LE_s) for DOY (left) 174 and (right) 182, created with the ALEXI model at 5-km resolution over the upper Midwest, and disaggregated to 120 (174) and 60 (182) m over the WC watershed with the DisALEXI algorithm. Gray cells have been flagged because of either cloud contamination or model convergence failure.

6. Conclusions

A simple technique has been described for quantifying vegetation clumping apparent at multiple scales and viewing angles over an agricultural landscape, using ground-based measurements of canopy architecture and maps of LAI created from Landsat visible/NIR imagery. Incorporation of the derived clumping indices into the TSM-based modeling system improves flux predictions at both the watershed and tower footprint scales for periods when the average fractional vegetation in the scene is around 50%. At the watershed scale, model performance has been assessed in comparison with spatially averaged flux measurements acquired with airborne- and tower-based EC systems, while disaggregated fluxes were compared directly

with flux data from individual towers. The inclusion of clumping effects reduces the overestimation of sensible heat resulting from an inaccurate assessment of the amount of bare soil visible to the thermal sensor providing the surface temperature inputs to the TSM.

While studied here in the context of the TSM, clumping may play a role in many thermal-based remote sensing models because it fundamentally affects the relationship between surface temperature, vegetation cover, and view angle. In future work, we will investigate the impact of integrating maps of vegetation clumping, derived from high-resolution VIS/NIR vegetation indices or POLDER/MODIS BRDF data, into an operational application of the ALEXI model over the continental United States.

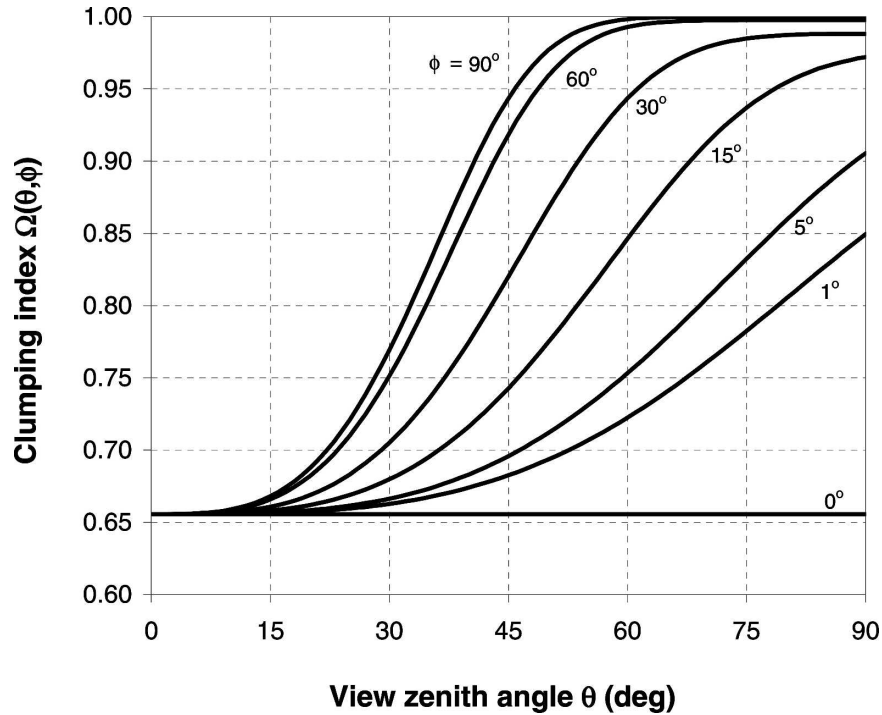


Figure A1. Model representation of apparent clumping index in corn and soybean row crops as a function of view zenith and azimuth angles (for case $f_{veg} = 0.5$ and $\bar{F} = 1.5$).

Acknowledgments. This work was sponsored by the National Aeronautics and Space Administration under Grants NAG1399008 and NNG04GK89G, and by the National Oceanic and Atmospheric Administration under Grant NA06GP0348. We appreciate the efforts of four anonymous reviewers, whose suggestions served to greatly improve the quality of this paper.

APPENDIX

Angular Dependence of Clumping Index in Row Crops

The dependence of the clumping index on zenith angle (θ) can be estimated with

$$\Omega(\theta) = \frac{\Omega_0 \Omega_{\max}}{\Omega_0 + (\Omega_{\max} - \Omega_0) \exp(k \theta^p)}, \quad (\text{A1})$$

where $p = 3.8 - 0.46D$, D is the ratio between the canopy height and the nominal clump width (h/w), and k depends on stand architecture but is approximately -2.2 for a wide variety of forest canopies (Kucharik et al. 1999). For the corn and soybean row crops sampled during SMACEX, the ratio of canopy width to height was near unity so that $p \sim 3.34$. In row crops and other anisotropic stands, the apparent clumping index will also vary azimuthally. Here, we suggest empirical forms

for azimuthal dependence in the parameters k and Ω_{\max} that reproduce the expected behavior of $\Omega(\theta, \phi)$.

The parameter k controls the response in clumping index to changing view zenith angle. In a row crop viewed perpendicular to the row ($\phi = 90^\circ$), Ω will vary slightly with increasing view zenith angle until the line of sight starts to increase a row, and will increase sharply thereafter (see Fig. A1). The cutoff zenith angle will decrease as the crop matures and the vegetated rows expand. This response was modeled over the full range in f_{veg} (0–1) based on simple geometric considerations, assuming that the row maintains a square cross section as f_{veg} (and, therefore, Ω_0) increases. A simple power-law equation for k as a function of Ω_0 was then fit to this modeled behavior, giving

$$k_{\perp} = -[0.3 + (1.7 \Omega_0)^{14}] \quad (\text{A2})$$

for azimuthal views perpendicular to the row.

Next, a functional form was found describing the expected variation of Ω_{\max} with azimuth angle (ϕ). We expect that Ω_{\max} will approach unity for an azimuth view perpendicular to the row ($\phi = 90^\circ$), and Ω_0 for a parallel view to the row ($\phi = 0^\circ$; i.e., no significant variation in Ω with zenith angle when viewed down the row, assuming the vegetation *in* the row is unclumped). Between these limits, geometric analysis leads us to a form

$$\Omega_{\max} = \Omega_0 + (1 - \Omega_0)(\sin\phi)^{0.05}. \quad (\text{A3})$$

Finally, we must adjust Eq. (A2) to incorporate an appropriate azimuthal dependence for k . For a given set of azimuths, we can estimate the expected cutoff zenith angle based on our idealized square row. As we move toward a lower ϕ (more parallel view), the cutoff occurs at increasingly higher values of θ , until at $\phi = 0$ there is no cutoff (see Fig. A1). The expected behavior can be reproduced with

$$k = -\{0.3 + [1.7 \Omega_0 (\sin\phi)^{0.1}]^{14}\}. \quad (\text{A4})$$

The above equations were developed based on 76-cm row spacing for corn and 38-cm row spacing for soybean.

REFERENCES

- Anderson, M. C., J. M. Norman, G. R. Diak, W. P. Kustas, and J. R. Mecikalski, 1997: A two-source time-integrated model for estimating surface fluxes using thermal infrared remote sensing. *Remote Sens. Environ.*, **60**, 195–216.
- , C. M. U. Neale, F. Li, J. M. Norman, W. P. Kustas, H. Jayanthi, and J. Chavez, 2004a: Upscaling ground observations of vegetation water content, canopy height, and leaf area index during SMEX02 using aircraft and Landsat imagery. *Remote Sens. Environ.*, **92**, 447–464.
- , J. M. Norman, J. R. Mecikalski, R. D. Torn, W. P. Kustas, and J. B. Basara, 2004b: A multiscale remote sensing model for disaggregating regional fluxes to micrometeorological scales. *J. Hydrometeorol.*, **5**, 343–363.
- Avissar, R., 1991: A statistical-dynamical approach to parameterize subgrid-scale land-surface heterogeneity in climate models. *Surv. Geophys.*, **12**, 155–178.
- , 1992: Conceptual aspects of a statistical-dynamical approach to represent landscape subgrid-scale heterogeneities in atmospheric models. *J. Geophys. Res.*, **97D**, 2729–2742.
- , and R. A. Pielke, 1989: A parameterization of heterogeneous land surface for atmospheric numerical models and its impact on regional meteorology. *Mon. Wea. Rev.*, **117**, 2113–2136.
- Berk, A., L. S. Bernstein, G. P. Anderson, P. K. Acharya, D. C. Robertson, J. H. Chetwynd, and S. M. Adler-Golden, 1998: MODTRAN cloud and multiple scattering upgrades with application to AVIRIS. *Remote Sens. Environ.*, **65**, 367–375.
- Blyth, E. M., 1995: Using a simple SVAT scheme to describe the effect of scale aggregation. *Bound.-Layer Meteorol.*, **72**, 267–285.
- Bonan, G. B., D. Pollard, and S. L. Thompson, 1993: Influence of subgrid-scale heterogeneity in leaf area index, stomatal resistance, and soil moisture on grid-scale land-atmosphere interactions. *J. Climate*, **6**, 1882–1897.
- Campbell, G. S., and J. M. Norman, 1998: *An Introduction to Environmental Biophysics*. Springer-Verlag, 286 pp.
- Chen, J. M., 1996: Optically-based methods for measuring seasonal variation of leaf area index in boreal conifer stands. *Agric. For. Meteorol.*, **80**, 135–163.
- , and T. A. Black, 1992: Defining leaf area index for non-flat leaves. *Plant Cell Environ.*, **15**, 421–429.
- , and J. Cihlar, 1995: Quantifying the effect of canopy architecture on optical measurements of leaf area index using two gap size analysis methods. *IEEE Trans. Geosci. Remote Sens.*, **33**, 777–787.
- , J. Liu, S. G. Leblanc, R. Lacaze, and J.-L. Roujean, 2003: Multi-angular optical remote sensing for assessing vegetation structure and carbon absorption. *Remote Sens. Environ.*, **84**, 516–525.
- Choudhury, B. J., N. U. Ahmed, S. B. Idso, R. J. Reginato, and C. S. T. Daughtry, 1994: Relations between evaporation coefficients and vegetation indices studied by model simulations. *Remote Sens. Environ.*, **50**, 1–17.
- Diak, G. R., W. L. Bland, and J. R. Mecikalski, 1996: A note on first estimates of surface insolation from GOES-8 visible satellite data. *Agric. For. Meteorol.*, **82**, 219–226.
- , —, —, and M. C. Anderson, 2000: Satellite-based estimates of longwave radiation for agricultural applications. *Agric. For. Meteorol.*, **103**, 349–355.
- Doraiswamy, P. C., J. L. Hatfield, T. J. Jackson, B. Akhmedoc, J. Prueger, and A. Stern, 2004: Crop condition and yield simulations using Landsat and MODIS. *Remote Sens. Environ.*, **92**, 548–559.
- Eidenshink, J. C., 1992: The 1990 conterminous U.S. AVHRR data set. *Photogr. Eng. Remote Sens.*, **58**, 809–813.
- French, A. N., J. M. Norman, and M. C. Anderson, 2003: Simplified correction of GOES thermal infrared observations. *Remote Sens. Environ.*, **87**, 326–333.
- Gao, B., 1996: NDWI—A normalized difference water index for remote sensing of vegetation liquid water from space. *Remote Sens. Environ.*, **58**, 257–266.
- Gillies, R. R., and T. N. Carlson, 1995: Thermal remote sensing of surface soil water content with partial vegetation cover for incorporation into climate models. *J. Appl. Meteorol.*, **34**, 745–756.
- Giorgio, F., and R. Avissar, 1997: Representation of heterogeneity effects in earth system modeling: Experience from land surface modeling. *Rev. Geophys.*, **35**, 413–437.
- Goudriaan, J., 1977: *Crop Micrometeorology: A Simulation Study. Simulation Monogr.*, Pudoc Center for Agricultural Publishing and Documentation, 249 pp.
- Hansen, M. C., R. S. Defries, J. R. G. Townshend, and R. Sohlberg, 2000: Global land cover classification at 1 km spatial resolution using a classification tree approach. *Int. J. Remote Sens.*, **21**, 1331–1364.
- Jackson, T., M. Cosh, and J. Famiglietti, 2003: SMEX02 Iowa regional ground soil moisture data. National Snow and Ice Data Center, Digital Media. [Available online at <http://nsidc.org/data/nsidc-0182.html>.]
- Koster, R., and M. Suarez, 1992a: A comparative analysis of two land surface heterogeneity representations. *J. Climate*, **5**, 1379–1390.
- , and —, 1992b: Modeling the land surface boundary in climate models as a composite of independent vegetation stands. *J. Geophys. Res.*, **97**, 2697–2715.
- Kucharik, C. J., J. M. Norman, L. M. Murdock, and S. T. Gower, 1997: Characterizing canopy nonrandomness with a Multi-band Vegetation Imager (MVI). *J. Geophys. Res.*, **102** (D24), 29 455–29 473.
- , —, and S. T. Gower, 1999: Characterization of radiation regimes in nonrandom forest canopies: Theory, measurements, and a simplified modeling approach. *Tree Physiol.*, **19**, 695–706.
- Kustas, W. P., and J. M. Norman, 1997: A two-source approach

- for estimating turbulent fluxes using multiple angle thermal infrared observations. *Water Resour. Res.*, **33**, 1495–1508.
- , and —, 1999a: Evaluation of soil and vegetation heat flux predictions using a simple two-source model with radiometric temperatures for partial canopy cover. *Agric. For. Meteor.*, **94**, 13–25.
- , and —, 1999b: Reply to comments about the basic equations of dual-source vegetation-atmosphere transfer models. *Agric. For. Meteor.*, **94**, 275–278.
- , and —, 2000a: Evaluating the effects of subpixel heterogeneity on pixel average fluxes. *Remote Sens. Environ.*, **74**, 327–342.
- , and —, 2000b: A two-source energy balance approach using directional radiometric temperature observations for sparse canopy covered surfaces. *Agron. J.*, **92**, 847–854.
- , J. L. Hatfield, and J. H. Prueger, 2005: The Soil Moisture–Atmosphere Coupling Experiment (SMACEX): Background, hydrometeorological conditions, and preliminary findings. *J. Hydrometeorol.*, **6**, 791–804.
- Lacaze, R., J. M. Chen, J.-L. Roujean, and S. G. Leblanc, 2002: Retrieval of vegetation clumping index using hot spot signatures measured by POLDER instrument. *Remote Sens. Environ.*, **79**, 84–95.
- Li, F., T. J. Jackson, W. P. Kustas, T. J. Schmugge, A. N. French, M. Cosh, and R. Bindlish, 2004: Deriving land surface temperature from Landsat 5 and 7 during SMEX02/SMACEX. *Remote Sens. Environ.*, **92**, 521–534.
- , W. P. Kustas, J. H. Prueger, C. M. U. Neale, and T. J. Jackson, 2005: Utility of remote sensing-based two-source energy balance model under low- and high-vegetation cover conditions. *J. Hydrometeorol.*, **6**, 878–891.
- MacPherson, J. I., and M. Wolde, 2002: NRC Twin Otter operations in the Soil Moisture-Atmosphere Coupling Experiment (SMACEX). National Research Council Canada Rep. LTR-FR-190, 91 pp.
- , —, W. P. Kustas, and J. H. Prueger, 2003: Aircraft and tower-measured fluxes over rapidly growing corn and soybean crops in central Iowa. Preprints, *17th Conf. on Hydrology*, Long Beach, CA, Amer. Meteor. Soc., CD-ROM, 3.1.
- Mason, P. J., 1988: The formation of areally-averaged roughness lengths. *Quart. J. Roy. Meteor. Soc.*, **114**, 399–420.
- McNaughton, K. G., and T. W. Spriggs, 1986: A mixed-layer model for regional evaporation. *Bound.-Layer Meteor.*, **74**, 262–288.
- Mecikalski, J. M., G. R. Diak, M. C. Anderson, and J. M. Norman, 1999: Estimating fluxes on continental scales using remotely-sensed data in an atmosphere-land exchange model. *J. Appl. Meteor.*, **38**, 1352–1369.
- Nash, L. E., and J. V. Sutcliffe, 1970: River flow forecasting through conceptual models—Part 1: A discussion of principles. *J. Hydrol.*, **10**, 282–290.
- Neale, C. M. U., and B. G. Crowther, 1994: An airborne multispectral video/radiometer remote sensing system: Development and calibration. *Remote Sens. Environ.*, **48**, 1–25.
- Nilson, T., 1971: A theoretical analysis of the frequency of gaps in plant stands. *Agric. Meteor.*, **8**, 25–38.
- Norman, J. M., and F. Becker, 1995: Terminology in thermal infrared remote sensing of natural surfaces. *Remote Sens. Rev.*, **12**, 159–173.
- , W. P. Kustas, and K. S. Humes, 1995: A two-source approach for estimating soil and vegetation energy fluxes from observations of directional radiometric surface temperature. *Agric. For. Meteor.*, **77**, 263–293.
- , and Coauthors, 2003: Remote sensing of surface energy fluxes at 10¹-m pixel resolutions. *Water Resour. Res.*, **39**, 1221, doi:10.1029/2002WR001775.
- Nouvellon, Y., M. S. Moran, D. Lo Seen, S. Rambal, D. Luquet, G. Chebouni, and Y. Inoue, 2000: PAR extinction in short-grass ecosystems: Effects of clumping, sky conditions and soil albedo. *Agric. For. Meteor.*, **105**, 21–41.
- Otkin, J. A., M. C. Anderson, J. R. Mecikalski, and G. R. Diak, 2005: Validation of GOES-based insolation estimates using data from the United States Climate Reference Network. *J. Hydrometeorol.*, **6**, 460–475.
- Priestley, C. H. B., and R. J. Taylor, 1972: On the assessment of surface heat flux and evaporation using large-scale parameters. *Mon. Wea. Rev.*, **100**, 81–92.
- Prueger, J. H., and Coauthors, 2005: Tower and aircraft eddy covariance measurements of water vapor, energy, and carbon dioxide fluxes during SMACEX. *J. Hydrometeorol.*, **6**, 954–960.
- Roujean, J.-L., and R. Lacaze, 2002: Global mapping of vegetation parameters from POLDER multiangular measurements for studies of surface-atmosphere interactions: A pragmatic method and its validation. *J. Geophys. Res.*, **107**, 4150, doi:10.1029/2001JD000751.
- Schuepp, P. H., M. Y. Leclerc, J. I. MacPherson, and R. L. Desjardins, 1990: Footprint prediction of scalar fluxes from analytical solutions of the diffusion equation. *Bound.-Layer Meteorol.*, **50**, 355–373.
- , J. I. MacPherson, and R. L. Desjardins, 1992: Adjustment of footprint correction for airborne flux mapping over the FIFE site. *J. Geophys. Res.*, **97**, 18 455–18 466.
- Twine, T. E., and Coauthors, 2000: Correcting eddy-covariance flux underestimates over a grassland. *Agric. For. Meteorol.*, **103**, 279–300.
- Vining, R. C., and B. L. Blad, 1992: Estimation of sensible heat flux from remotely sensed canopy temperatures. *J. Geophys. Res.*, **97** (D17), 18 951–18 954.
- Walthall, C., W. Dulaney, M. C. Anderson, J. M. Norman, H. Fang, and S. Liang, 2004: A comparison of empirical and neural network approaches for estimating corn and soybean leaf area index from Landsat ETM+ imagery. *Remote Sens. Environ.*, **92**, 465–474.
- Wieringa, J., 1986: Roughness-dependent geographical interpolation of surface wind speed averages. *Quart. J. Roy. Meteor. Soc.*, **112**, 867–889.
- Wilson, K., and Coauthors, 2002: Energy balance closure at FLUXNET sites. *Agric. For. Meteorol.*, **113**, 223–243.
- Zhan, X., W. P. Kustas, and K. S. Humes, 1996: An intercomparison study on models of sensible heat flux over partial canopy surfaces with remotely sensed surface temperatures. *Remote Sens. Environ.*, **58**, 242–256.